COLOR FLUX DISTRIBUTION ON THE LATTICE*

BY R. W. HAYMAKER

Department of Physics and Astronomy, Louisiana State University, Baton Rouge, LA 70803, USA

AND J. WOSIEK

Chair of Computer Science, Jagellonian University, Cracow**

and

Max-Planck-Institut für Physik und Astrophysik, Werner-Heisenberg-Institut für Physik, P.O. Box 401212, Munich, West Germany

We describe the work by· the Cracow-LSU collaboration on Chromoelectric and chromomagnetic flux distributions around the static charges. We find that large cancellations between electric and magnetic energy density lead to a narrow flux tube.

PACS numbers: 11.15.Ha

1. Introduction

I would like to report on progress in measuring non-abelian flux distributions in the presence of static charges in lattice gauge theory in four dimensions. Projects are underway on SU(2) and SU(3) by a number of people: Jacek Wosiek and Andrzej Kotanski at the Jagellonian University and Yingcai Peng, Vandana Singh and myself at Louisiana State University. Here I will describe the flux problem for $q\bar{q}$ in SU(2) for quark separations of up to 9 lattice units. Although the basic picture of a flux tube between a heavy quark-antiquark pair is well established, the detailed distribution of the flux is just now being elucidated. Early work on this problem was done by Fukugita and Niuya [1] and Flower and Otto [2]. More complete study for SU(3) were done by Sommer for the $q\bar{q}$ separation up to four lattice units [3]. In 1987 we have computed the electric parallel component of the SU(2) flux for the square Wilson loops reaching the $q\bar{q}$ distance of six lattice units [4]. Jorysz and Michael [5] have studied an external adjoint source in SU(2). Sommer [6]

** Address: Instytut Fizyki UJ, Reymonta 4, 30-059 Kraków, Poland.

investigated thoroughly all flux components for SU(2) using Polyakov lines as sources for quark separations up to four lattice units.

Here we present results for all six components of the color field with particular emphasis on filtering out contributions from excited states. This is done for the $q\bar{q}$ separations up to six lattice units. We shall also present some results for yet larger (seven to nine lattice units) distances. In this case however, contamination by the higher states of the color field cannot be entirely disentangled.

One of the interesting results in these studies [6] is that there are large cancellations between electric and magnetic components of the energy distribution giving a much thinner flux tube than one would estimate based on a single component. This effect is now clearly seen for the well developed $q\bar{q}$ tube.

There are many complications beyond the lattice granularity in trying to develop a picture of color fields comparable to the highly intuitive classical electric and magnetic field lines. The self interactions of these fields play a central role which destroys the linearity of the problem. In addition, only squares of the individual field components are meaningfull in the nonabelian theory hence the concept of the field lines has limitted application. Quantum fluctuations pose further restrictions on the simple classical analogy. One is primarily interested in the continuum limit and hence in the scaling and renormalization of the lattice results. It is known that the energy density scales accordingly to its canonical dimension *mass*[4] while the gluon condensate $F_{\mu\nu}^2$ does not [8]. Hence the behaviors of the electric and magnetic components separately are to large extent reflecting the lattice regularization. When wieved in this context, the intriguing result that the chromomagnetic energy density is negative[1] (relative to the vacuum), may not be meaningfull physicaly. Still we believe that the fact that the magnetic and electric contributions have the *opposite* signs is significant.

Having all the above reservations in mind, let us nevertheless digress briefly to look at classical euclidean continuum electrodynamics. Of course there is no flux tube in this example. The purpose of this exercise is nothing more than to fix the notation and provide some framework to classify our results obtained for the non-abelian quantum theory. In our investigations we employ Wilson loops to represent the world lines of the heavy $q\bar{q}$ sources. It is then necessary to extrapolate to loops with large time extent to suppress the effects of creation and annihilation of charges. Consider a current as shown in Fig. 1. The electromagnetic potential is

$$A^\mu(x) = \frac{4\pi}{c} \int G_E(x-x')J^\mu(x')d^4x'. \tag{1}$$

The effect of finite T is to give finite magnetic components of the electromagnetic field $F^{13} = -B_2$ and $F^{23} = B_1$. These are the transverse components, $B_\perp$. For large T the effects of creation and annihilation are negligible, $B_\perp$ dies away leaving an electrostatic field. Note however that no longitudinal component of magnetic field is ever generated, $F^{12} = B_3 = 0$. For the non-abelian problem, all components are of the same order of

---

[1] It was first emphasized by Sommer [3] and is fully confirmed by our present simulations.

$$-\delta^{\mu,3}\delta(x_4-\tfrac{T}{2})\delta_\perp^2(x_\perp)$$

$$-\delta^{\mu,4}\delta(x_3+\tfrac{R}{2})\delta_\perp^2(x_\perp) \qquad \delta^{\mu,4}\delta(x_3-\tfrac{R}{2})\delta_\perp^2(x_\perp)$$

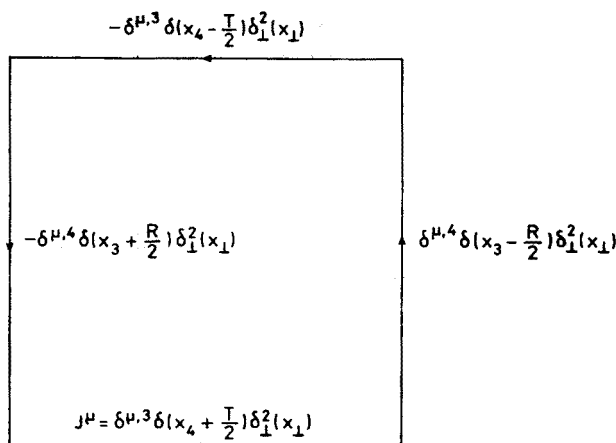$$J^\mu=\delta^{\mu,3}\delta(x_4+\tfrac{T}{2})\delta_\perp^2(x_\perp)$$

Fig. 1. Wilson loop source

magnitude, for all loop sizes, and do not show the relations exhibited here. The one similarity is that the E_z is always the largest and B_z is always the smallest.

In Section 2 we give a few details of the simulation, in Section 3 we report on general features of the data for the heavy quark potential and the flux. In Section 4 we look at sum rules, both the sum of flux on a slice transverse to the flux tube, and the Michael sum rules [8] for the volume integral of the flux. It is here where the electric-magnetic cancellation is most clear.

2. Simulation

Lattice observable needed to measure the flux is the following

$$e^{\mu\nu}(x) = \frac{\beta}{a^4}\left(\frac{\langle WP_x^{\mu\nu}\rangle}{\langle W\rangle}-\langle P\rangle\right) \simeq \frac{\beta}{a^4}\left(\frac{\langle WP_x^{\mu\nu}-WP_\infty^{\mu\nu}\rangle}{\langle W\rangle}\right), \tag{2}$$

where W is the Wilson loop, $P_x^{\mu\nu}$ the plaquette located at x and a is the lattice spacing. In the classical continuum limit

$$e^{\mu\nu} \xrightarrow{a\to 0} -\tfrac{1}{2}\langle(F^{\mu\nu})^2\rangle_{q\bar{q}-\text{vac}}, \tag{3}$$

where the notation $\langle\,.\,\rangle_{q\bar{q}-\text{vac}}$ means the difference of the average values in the $q\bar{q}$ and vacuum state. From now on we shall be using field components in the Minkowski space and hence

$$e^{\mu\nu} \to \tfrac{1}{2}(-B_1^2, -B_2^2, -B_3^2; E_1^2, E_2^2, E_3^2). \tag{4}$$

Correspondence between various components and $e^{\mu\nu}$ is standard and is also shown in Figs 1 and 2 ($z = x_3$, $\tau = x_4$). The energy density is

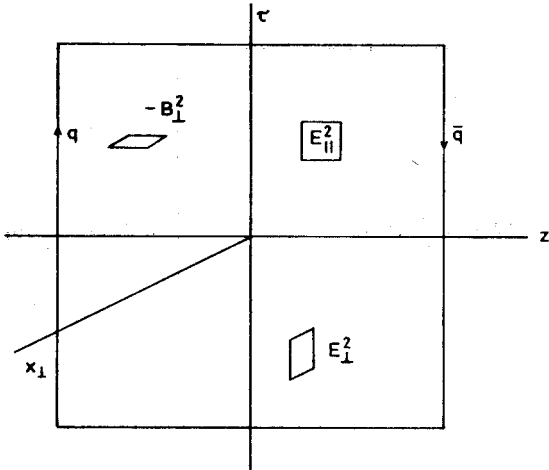$$\tfrac{1}{2}\varepsilon = \tfrac{1}{2}(E^2+B^2). \tag{5}$$

Fig. 2. Correspondence between plaquettes and components: space-time

Since however magnetic contribution turns out to be negative, there is a strong cancellation between the two terms.

The computations were done on the FPS AP264 array processor at LSU. Our lattice size was a $17^3 \times 20$ hypercube with helical boundary conditions based on a configuration program made available to us by Mike Creutz. Updating was done checkerboard fashion which requires space dimensions odd and the time dimensions even. We also use Creutz's overrelaxation algorithm [9] alternated with a one or two hit Metropolis in order to decrease sweep to sweep correlations. For SU(2) overrelaxation is microcanonical and hence Metropolis is needed to sample configurations with different energies/actions. We measured all rectangulat loop sizes from 1×1 to 6×9. Because of the large amount of data generated and because of the difficulty of getting good statistics, the data was folded on rectangular symmetry planes. We also limited the measured flux to a fiducial volume consisting of a closed volume surrounding the Wilson loop four lattice spacings in every direction. We measured all six components of the flux.

Table 1 gives the parameters for our measurements. The physical values of the lattice constant were taken from Refs [6, 7], these numbers are also consistent with our analysis of Wilson loops. As was already mentioned, Wilson loop represents (classically) the world line of the external source. Quantum mechanically it provides the projection into the

TABLE I

Parameters used in simulation

β	a lat. spacing	N_{therm}	Sweeps between meas.	No. of meas.
2.5	0.09 fm	2200 ovrrl., 2200 metr.	5 ovrrl. 5 metr.	200
2.4	0.13 fm	1700 ovrrl., 1700 metr.	5 ovrrl. 5 metr.	230
2.3	0.17 fm	2862 ovrrl., 2862 metr.	5 ovrrl. 5 metr.	240

$q\bar{q}$ sector of the Hilbert space. Projection onto the ground state of the $q\bar{q}$ string is achieved only when the time extent of the loop tends to infinity. On the other hand the interest lies in the shape of the flux tube for large *space* separations. However the large space and time separations are very difficult to achieve simultaneously because of the exponential suppression of the signal with the area of the loop. For that reason the straightforward measurement of these quantities would lead to prohibitive computer time or intolerable errors. Enhancements of the measurements are essential to beat down the errors.
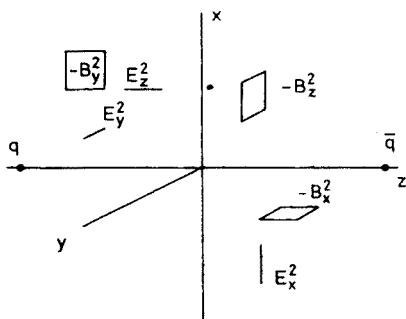

Fig. 3. Correspondence between plaquettes and components: space

One enhancement is almost trivial but contributed significantly in reducing errors [4]. That is indicated in the second part of Eq. (2) in which the flux is measured relative to a point at infinity. This does not change the lattice average but the main fluctuations of PW, which are due to the Wilson loop itself, cancel when the difference, Eq. (2), is computed configuration by configuration. By taking a point where the correlation vanishes the two forms in Eq. (2) are equal. In practice we take a corner of the hypercubic fiducial volume as the point at infinity.

The second important enhancement was to do as many integrals analytically as is practical. For example the one link integral can be done using

$$\int [dU] U e^{\frac{\beta}{2} \text{tr}[UK^\dagger]} = \frac{I_2(\beta b)}{I_1(\beta b)} V \int [dU] e^{\frac{\beta}{2} \text{tr}[UK^\dagger]}, \tag{6}$$

where K is the sum of six 'staples' coupling to given U in the action [10]. The sum of SU(2) matrices in the $j = \frac{1}{2}$ representation is a multiple of an SU(2) matrix which we denote by V

$$K = bV; \quad b \equiv (\det K)^{1/2}. \tag{7}$$

The effect of Eq. (6) when applied to a simulation is to replace a link U occurring in the Wilson loop by a corresponding sum of 'staples' K. This is indicated in Fig. 4. Since K involves 18 links, one can expect the fluctuations of the ensemble of K's to be suppressed compared to a single link U in each measurement.

This result is useful as long as subsequent analytic integration does not involve one of the links in K. For example, for the potential measurement, this will work for those links that make up the sides of a Wilson loop of size 2×2, or larger, as long as one link
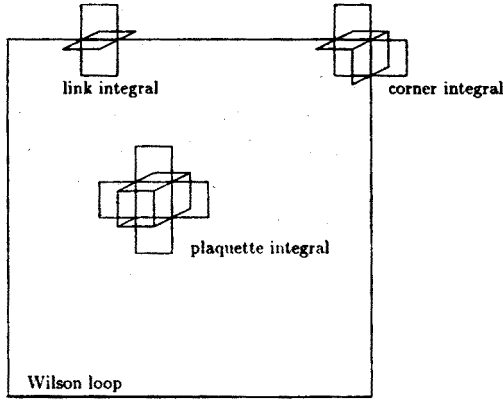
Fig. 4. Links involved in link, corner and plaquette integrals

on each corner is left in its original form. This result must be generalized to handle the four links in a plaquette and the the two links that form corners. This has been done by B. Bunk [12] in an unpublished report which he kindly made available to us.

To do the plaquette integral consider the following four-link integral

$$Z(\gamma, \beta) \equiv \int [dU_1 dU_2 dU_3 dU_4] e^{-S}, \tag{8}$$

where

$$-S \equiv \left(\frac{\gamma}{2} \operatorname{tr} [U_4^{\dagger} U_3^{\dagger} U_2 U_1] + \frac{\beta}{2} \sum_{k=1}^{4} \operatorname{tr} [U_k K_k^{\dagger}] \right). \tag{9}$$

We can reduce this four link integral to a single sum using SU(2) character expansions. The result is

$$\int \left[\prod_l dU_l \right] \frac{1}{2} \operatorname{tr} (U_4^{\dagger} U_3^{\dagger} U_2 U_1) e^{-S} = \frac{\left. \dfrac{\partial Z(\gamma, \beta)}{\partial \gamma} \right|_{\gamma = \beta}}{Z(\beta, \beta)} \int \left[\prod_l dU_l \right] e^{-S}, \tag{10}$$

where

$$Z(\gamma, \beta) = \sum_j c_j(\gamma) \frac{(2\pi^2)^4}{(2j+1)^4} \prod_{k=1}^{4} c_j(\beta b_j) \chi^{(j)}(V_4^{\dagger} V_3^{\dagger} V_2 V_1). \tag{11}$$

The c's are coefficients of the expansions of the Boltzman factor in characters of SU(2), $\chi^{(j)}(V)$. Full details will be given elsewhere. By doing the link integrals in a plaquette, the result is expressed in terms of the links pictured in Fig. 4. Again the value of the plaquette is spread over many more links and the subsequent simulation will see a smaller sweep to sweep spread in the values of this 'fat' operator. Similarly one can perform the corner integral. Details are in the Appendix.

In the vectorized code, we save the long vectors of Wilson loops (or fat Wilson loops) corresponding to all locations of the loop and similarly for all locations and orientations of the plaquette. We then calculate the cross correlation between these two long vectors. To do a naive correlation measurement an estimate of computer time T, gives

$$T \propto V_{\text{lattice}} \times V_{\text{fiducial}}, \tag{12}$$

whereas if one employs fast Fourier transforms we obtain

$$T \propto V_{\text{lattice}} \times \ln_2 (V_{\text{lattice}}). \tag{13}$$

Given the size of our fiducial volume, the fast Fourier transform was essential to beat down computer time.

The fast Fourier transforms give all the correlations, not just those in the fiducial volume. However, when the fat operators indicated in Fig. 4 get too close together, the analytic expressions, derived for the case of nonoverlapping links, break down. Therefore one must recalculate those correlations, dropping the analytic integrations for one or the other or both operators. As a consequence self energies, i.e. correlations when plaquette is touching the Wilson loop, are harder to measure than more distant correlations. When a link of a plaquette overlaps a link of the Wilson loop analytic integrals must be dropped on both operators. Correlations measured with completely unenhanced operators have unacceptable errors. Measurements of self energies with an improved treatment will be reported later.

3. Results

3.1. Potential

The energy of the static $q\bar{q}$ sources in the SU(2) gauge theory was studied by many authors and is fairly well known [11, 6, 7]. This provides us with rather stringent tests of our data and the error reduction technique. Our results for the Wilson loops are consistent with the published raw results of Gutbrod [11] which were obtained for the icosahedral subgroup of SU(2). Typically statistical errors are smaller by a factor of 4 for large (5×7 for $\beta = 2.4$) loops.

The static potential of the $q\bar{q}$ pair is identified with the lowest eigenvalue $V_0(R)$ of the lattice hamiltonian projected onto the $q\bar{q}$ sector.

$$\langle W(R, T) \rangle = \frac{1}{Z} \text{Tr} \left(\mathcal{T}^{N_t - T/a} S P_{q\bar{q}} \mathcal{T}^{T/a} S \right)$$

$$= \sum_i \mathcal{R}_i \exp \left(-T E_i(R) \right) \xrightarrow{T \to \infty} \mathcal{R}_0 \exp \left(-T E_0 \right), \tag{14}$$

where $a E_i(R) = \ln (\lambda_{\text{vac}}/\lambda_i)$, λ_i and λ_{vac} being the eigenvalues of the transfer matri $\mathcal{T}$ in the $q\bar{q}$ and the vacuum sector respectively. S is the operator which excites the $q\bar{q}$ states from the vacuum and $P_{q\bar{q}}$ denotes the projector onto the $q\bar{q}$ sector of the Hilbert space.
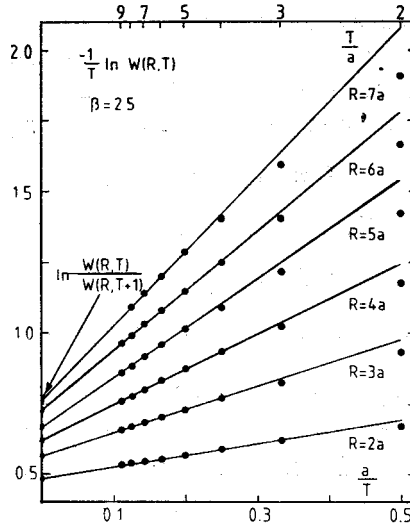
Fig. 5. Dependence of the $\dfrac{-1}{T}$ ln $\langle W(R, T)\rangle$ on $\dfrac{1}{T}$. Excited states cause deviation from the straight line on this plot

R and T are the space and time extents of the Wilson loop in the physical units, a is the lattice constant and $Z = \mathrm{Tr}(\mathscr{T})^{N_t})$. Customarily one fits, for fixed R, the time dependence of $\langle W(R, T)\rangle$ assuming domination of the first few (usually two to three) states in the sum of Eq. (14). Before doing that however, let us slightly rearrange our data in order to get some idea on how important are contributions from higher states, and how relevant is the extrapolation to large T/a values. Upon rewriting the Eq. (14) one has ($V_i(R) \equiv E_i$)

$$- \frac{1}{T} \ln \langle W(R, T)\rangle = V_0(R) - \frac{1}{T} C(T), \qquad (15)$$

where $C(T)$ contains the contribution from higher states

$$C(T) = \ln R_0 + \ln \left(1 + \sum_i \frac{R_i}{R_0} \exp\left(-T(V_i(R) - V_0(R))\right)\right). \qquad (16)$$

For large T, contribution from higher states is small and $C(T)$ becomes independent of T. Hence plotting the $\dfrac{-1}{T}$ ln $\langle W(R, T)\rangle$ versus $\dfrac{1}{T}$ gives us a good idea about the uncertainities of the extrapolation needed to extract the lowest potential $V_0(R)$. Figure 5 shows such a plot for a range of R/a values and for $\beta = 2.5$. The dependence is indeed approximately linear for $T/a > 3$ showing that the lowest state dominates the sum, Eq. (14), rather early. Moreover, the extrapolated value for the intercept agrees nicely with the "time dependent" estimate $V_{es}(R) = \ln(\langle W(R, T)\rangle / \langle W(R, T+1)\rangle)$ for the potential[2]. Finally, we have

---

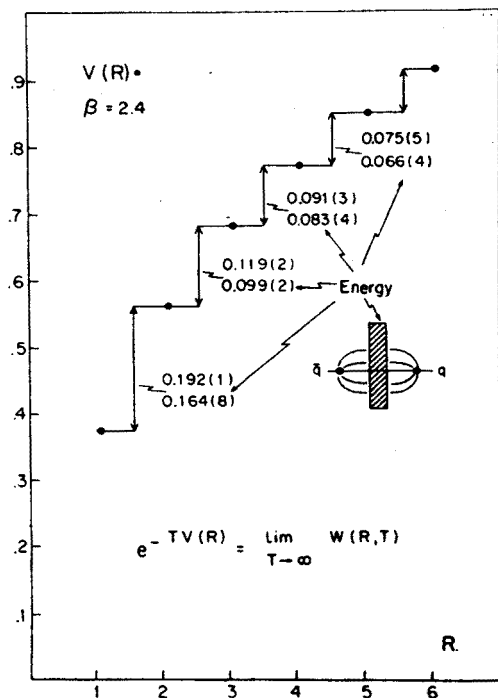[2] V_{es} varies in the range covered by the size of the dots on the Y axis.

Fig. 6. Heavy quark potential in lattice units. The upper numbers are the differences between the potential at neighboring points. The lower numbers are obtained from the transverse energy sum rule described in Section 3.3

fitted the time dependence using the formula (14) with two and three states contributing to the sum. The fit was always (for all R's and β's) satisfactory and the lowest eigenvalue was stable against changing the number of parameters in the fit. Resulting values for $V_0(R)$ agree very well with the intercepts as shown in Fig. 5. They are also plotted in Fig. 6 for $\beta = 2.4$.

The detailed discussion of the scaling of the potential will be published elsewhere, we do not expect that it will reveal any new features of the nonperturbative beta function since this range of parameters was already carefully studied in the literature. Our preliminary analysis of the potential shows scaling and gives the values for "running" lattice constant which are consistent with the results of Refs [6, 7].

We have probed the $q\bar{q}$ distances up to 1.2 fm, however our data allow also to extract the qualitative features of the confining potential for the yet larger separations of the static sources. Our rectangular loops contain the information on the potential for distances up to $R/a = 9$ which corresponds to $R = 1.5$ fm at $\beta = 2.3$. Extraction of the lowest state is however subject to the systematical error because only the limited range of T values is available ($T_{max}/a = 5$) and hence the contamination with higher states is bigger. Nevertheless results of the fit show that the $q\bar{q}$ potential keeps growing between 1.2 and 1.5 fm and the slope is consistent with the string tension extracted from smaller separations.

3.2. Flux — general behavior

Let us start the discussion of flux by looking at the value of the correlation at the center of the Wilson loop as a function of spatial extent, R and time extent T. These are shown in Fig. 7. The central value gives the flux at the midpoint between the quarks and for the middle time slice. Fig. 7 shows how well the flux data extrapolates to large T for various R's. The largest component $E_\parallel$ consistently has the strongest T dependence. For small R's,
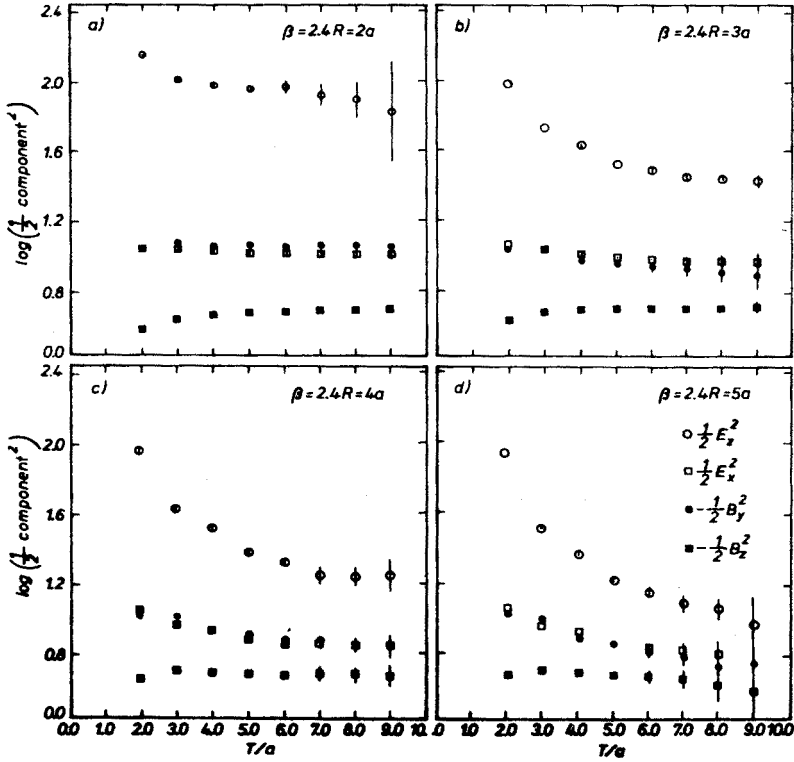

Fig. 7. Flux at the center of the Wilson loop in lattice units as a function of T, for $R = 2a-5a$. Ordinate is $\log_{10}$ of components indicated, $\beta = 2.4$

where the errors are negligible, the other components are approximately constant for $T \geqslant 5$. This is the first indication that one does not need to go to very large T to get reliable data, at least for these components. Data for small T/a (or R/a) $= 2, 3$ show clearly the lattice granularity. Only for larger sizes of the Wilson loop these artifacts die away and the points shown in Fig. 7 lie on the smooth curves. We are presently exploiting the transfer matrix formalism, fitting all components to exponential forms in T in order to extrapolate to large times. This will be reported later.

The suppression of errors in $E_\parallel$ in Figs. 7b–d vs Fig. 7a is due to the use of the fat Wilson loop, vs the simple loop. Since the errors increase with increasing T and R, the simple loops would clearly lead to unacceptable errors. The smallest component $B_\parallel$ always uses fat operators, and hence always has the smallest errors.
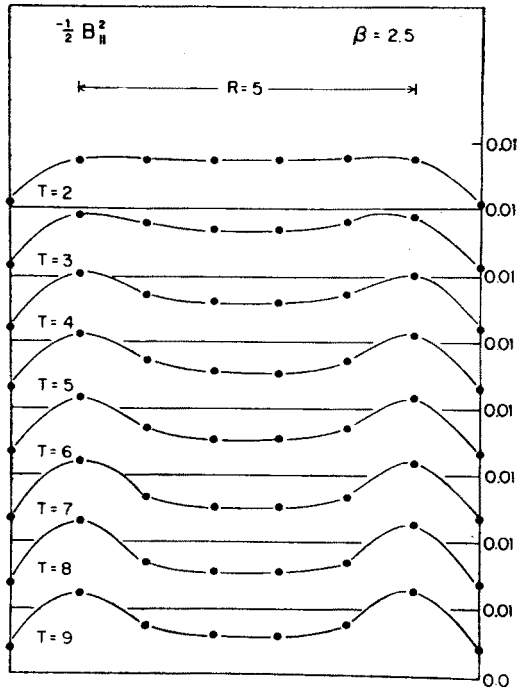
Fig. 8. Time dependence of longitudinal profile of the $B_{\parallel}$ component. Lattice units, $\beta = 2.4$
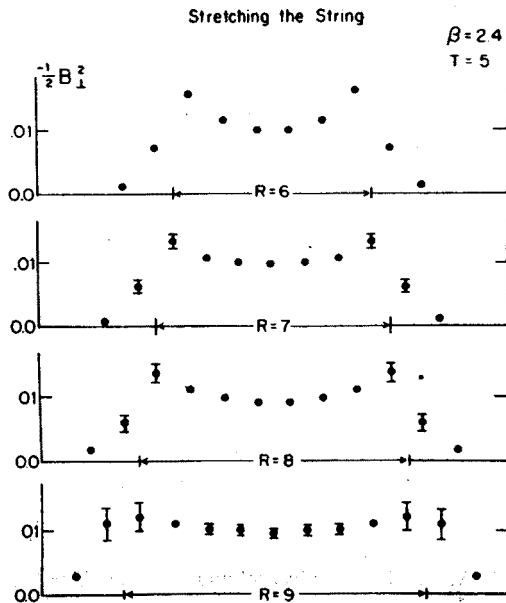

Fig. 9. Dependence of the longitudinal profile of the $B_{\perp}$ on the $q\bar{q}$ distance. Lattice units, $\beta = 2.4$

Fig. 8 shows the high quality of the $B_{\parallel}$ data. Shown is the profile of the $B_{\parallel}$ component along the axis connecting the charges for T from $2a$ to $9a$. Clearly it is not necessary to take T larger than $4a$ or $5a$ here. Fig. 9 looks at the $B_{\perp}$ component as one stretches the string between the quarks from $R = 6a$ to $9a$. Finally we show in Fig. 10 all the components for large $R(= 8a)$ and $T = 5a$. The points surrounding the charges are off scale and with very large errors.

Fig. 11 shows the values of the flux at the mid-point of the flux tube as a function of quark separations up to $R = 9a$, in physical units, for $\beta = 2.4$. These were all done for
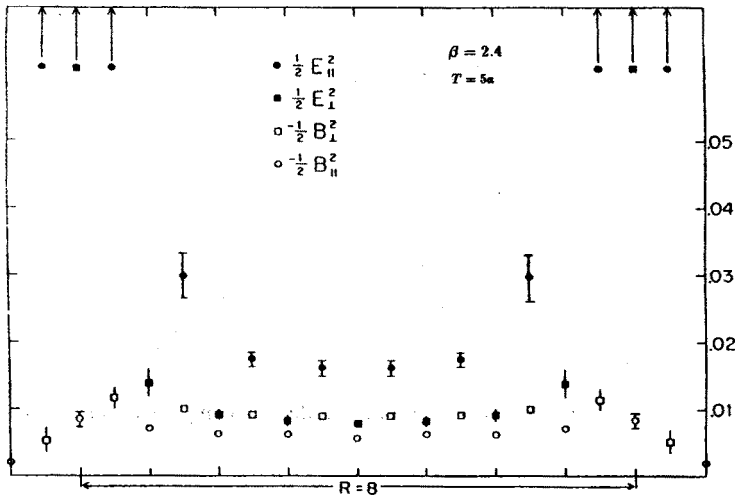

Fig. 10. Longitudinal profile of all components for $T = 5a$ and $R = 8a$. Lattice units. Self-energy points are off the scale and with large errors
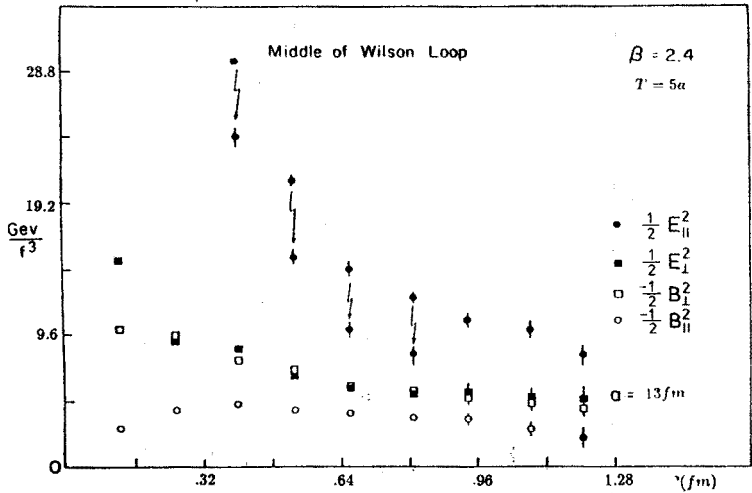

Fig. 11. Flux at the center of the Wilson loop in physical units for fixed $T = 5a$, and for $R = 1$ to 9 lattice units. Measurements were taken for larger T but only for $R < 6a$. Arrows indicate the values of the flux for $T = 9a$. Only the $E_{\parallel}$ points were affected

$T = 5a$. For all but the 3 largest R's, we have data for larger T. Increasing T up to $9a$ changes only the $E_\parallel$ component and the change resulting from increasing T to $9a$ is indicated with the arrows.

From Fig. 11 we can get a very crude estimate of the energy density at the center point of the flux tube [13]. Even though the electric and magnetic contributions subtract, it is evident that the asymptotic value for the energy density is much bigger than the typical density in the MIT bag model [14] $\varepsilon_{MIT} = 4B_{MIT} = 0.2$ GeV/fm³. In another words, confining tube generated by the nonabelian interactions is much more narrow than the MIT tube
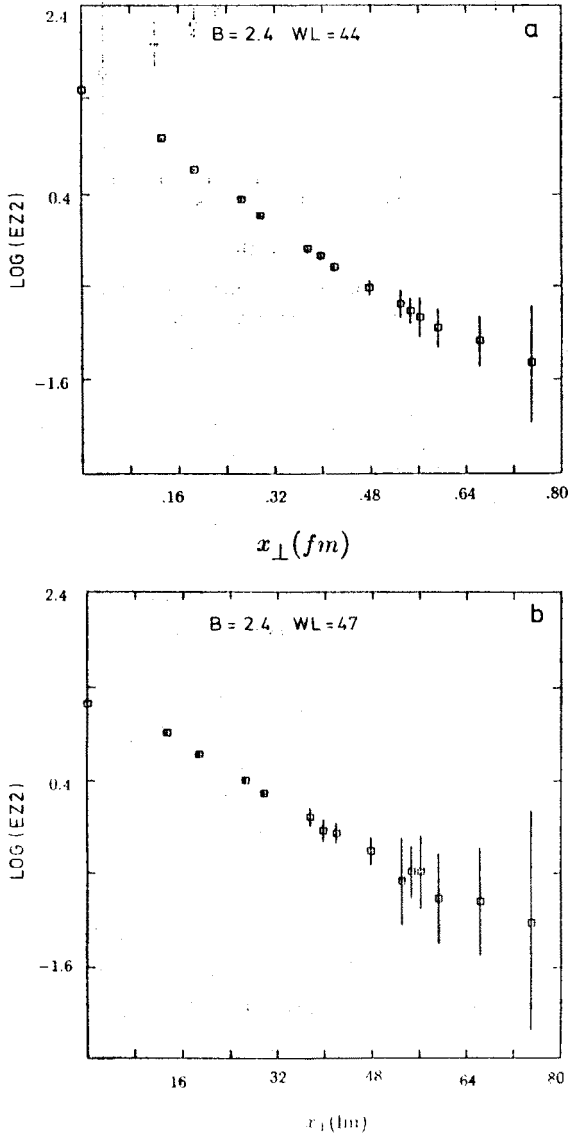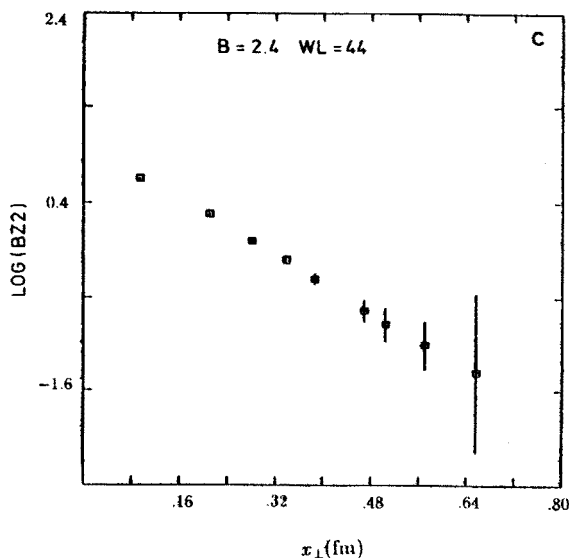

Fig. 12

Fig. 12. Transverse profiles of the flux tube for the components at the midpoint, as a function of distance in fermis. Ordinate is $\log_{10}$ (component of energy density in units GeV/f^3). Fig. 12a: $R = 4a$, $T = 4aE_z$ component; Fig. 12b $R = 4a$, $T = 7a$, E_z component; Fig. 12c: $R = 4a$, $T = 4a$ B_z component

[15]. Therefore it is unlikely that a volume energy alone can account for the cavity states, and at the same time give enough pressure to squeeze the flux into such a narrow tube. Since the errors are still large, we are not able to confront the discrepancy more quantitatively at the moment, however it seems unprobable that our estimates are off by a factor of 20. More carefull estimate of the asymptotic value for ε will be soon reported. Also the sum rules of the next section will lead us to the similar conclusion.

One of our primary goals in this work is to explore the shape of the flux tube. In particular we look at the transverse shape of the tube at the middle time slice, and at the z slice mid-way between the quarks. Figs. 12 show the typical behavior of individual components plotted against the transverse distance. Except for a small rounding at the point on the axis, they are all consistent with exponential behavior, presumably determined by the lowest glueball mass. Figs. 12a and 12b contrast the data increasing T from $4a$ to $7a$. Figs. 12a and 12c contrast different components.

3.3 Flux — sum rules

There is a very interesting check on our flux data provided by sum rules derived by Michael [8]. The energy it takes to pull quarks apart as measured by the potential must be accounted for by an energy density integrated over all space. The lattice version is the Michael energy sum rule.

$$\tfrac{1}{2} \sum_{\vec{x}} a^3 [E^2(\vec{x}) + B^2(\vec{x})] = V(R) + \frac{f(\beta)}{a} . \tag{17}$$

Recall that the measured magnetic component of the energy is negative. Therefore there is a cancellation in Eq. (17) in calculating energy. To test this relation, we need to sum over all space. Unfortunately we have very poor data for plaquettes that touch the Wilson loop. We will assume that these contributions are approximately independent of the separation R and discard them. Hence we can check the R dependence of Eq. (17) up to a constant. The results are shown in Fig. 13. Errors preclude a definitive check but the behavior is correct.
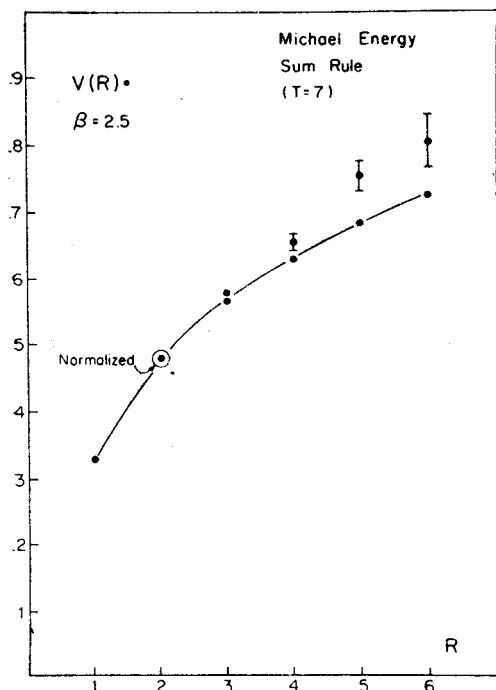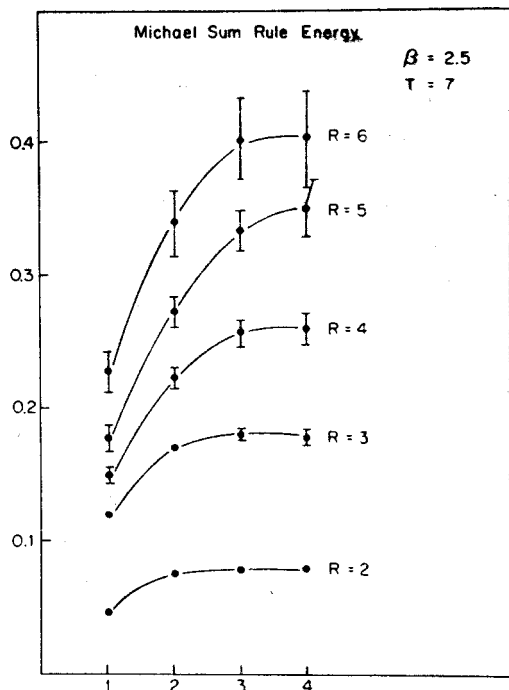

Fig. 13

Fig. 14

Fig. 13. Test of Michael volume energy sum rule up to a constant. Self energies were discarded and the value normalized at $R = 2a$

Fig. 14. Test of the fiducial volume dependence of the Michael volume energy sum rule for a fiducial volumes of 1 to 4 lattice units surrounding the Wilson loop

A rather important test of the volume sum of flux is to see if our fiducial volume is large enough. Fig. 14 gives the sum rule as a function of fiducial volume. The value 4 is the maximum volume we measured, being a closed region of 4 lattice units in all directions surrounding the Wilson loop. Fig. 14 shows the effect of dropping back to 3, 2, and 1 lattice units. Hence 4 units is clearly adequate.

There is a second sum rule for the gluon condensate:

$$\frac{1}{2} \sum_{\vec{x}} a^3 [E^2(\vec{x}) - B^2(\vec{x})] = -\beta \frac{\partial \ln a}{\partial \beta} V(R) - \frac{\beta}{a} \frac{\partial f}{\partial \beta}. \tag{18}$$

We attempted to measure this quantity. However, because there is no cancellation between electric and magnetic components this extends over a much larger volume and we do not have a large enough fiducial volume to test the sum rule. Similar effect is seen by Jorysz and Michael for the single adjoin source [5].

The general picture of the flux tube leads to another sum rule that is much simpler to measure. Rather than looking at the potential itself, let us look at the work required to pull a $q\bar{q}$ apart by one lattice spacing. The potential rises by this quantity of work. If the effect is merely to stretch the flux tube, leaving the end configurations unchanged, then we should be able to account for this work by a volume integral of the flux over a transverse slice of the string one lattice spacing thick at for example the mid-point of the tube. Fig. 5 gives the result. The upper numbers at each step are the differences between the potential as R increases by 1 unit. The lower number is the result from the transverse sum rule. For small R the flux tube is just forming, and the agreement is poor. For a well formed flux tube, $R = 4$, 5, the agreement is good.

Again we need to do a test of the fiducial volume. This is shown in Fig. 15. The important result is that the sum rule is being saturated within the fiducial volume of one lattice unit surrounding the $q\bar{q}$ axis. For large separations, $R = 5a$, $6a$ the sum rule is saturated between 1 and 2 lattice units. In none of these cases do we need 3 or 4 units. The cancella-
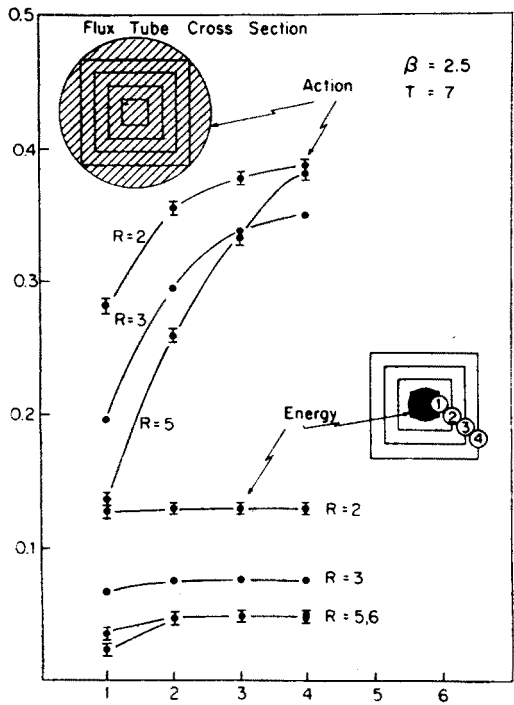

Fig. 15. Fiducial volume dependence of energy and gluon condensate sum rules measured on the transverse slice of the flux tube at the midpoint. The shaded areas contrast the small size of the energy flux compared to the gluon condensate

tion is rather dramatic. The gluon condensate sum rule is again quite a different matter. For this case there is no cancellation and the fiducial volume dependence is totally different. And for $R \geqslant 4a$ the measured fiducial volume is clearly inadequate. As indicated in Fig. 15 the shaded area in each case indicates schematically the region required to saturate the sum rule.

Our results on the smallness of the flux tube are consistent with Sommer's result [6]. If we take Sommer's value for $-\beta \dfrac{\partial \ln a}{\partial \beta} \approx 10$ we are consistent with the gluon condensate sum rule being about a factor of 10 larger than the energy.

Let us use this transverse energy sum rule to estimate independently the energy density at the mid-point of the flux tube. First in lattice units, the total energy in a transverse slice, taken from Fig. 5 is $\approx 0.07 \, a^{-1}$. As a conservative estimate, take the radius of the flux tube to be 2 lattice units. Then the energy is spread over a volume of $\pi(2a)^2 a$. Therefore in physical units (running lattice constant $a(2.4) = 0.13 \, \text{fm}$)

$$\text{Energy density} \simeq 0.0056 a^{-4} \simeq 4 \, \frac{\text{GeV}}{\text{fm}^3} . \tag{19}$$
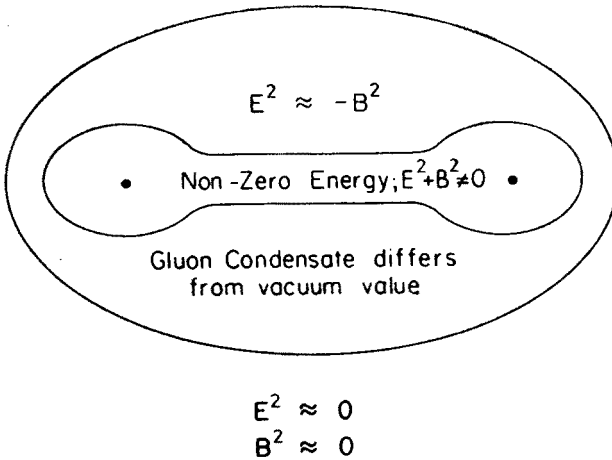
This number roughly agrees with what can be inferred from Fig. 11. Both methods however introduce large uncertainties. Improving this estimate requires carefull extrapolation of the time dependence as well as taking into account different space location of each field component.

One of the consequences of the cancellation discussed above, is that we know very little about the shape of the flux tube since it is contained in a size comparable to the lattice spacing. Although the individual components have a very clear exponential behavior as shown in Fig. 12, the underlying energy distribution need not be exponential. We are not yet in a position to see if the profile is gaussian [16, 17]. It should be stressed however, that Lüscher asymptotic prediction was calculated for the single $E_{\parallel}$ component.

4. Summary and conclusions

Figure 16 gives our major conclusions. The presence of heavy quark sources distorts the gluon condensate from its vacuum value in a large region around the quarks. However there is a conspiracy among the electric and magnetic contributions to the energy to cancel everywhere except in the neighborhood of the charges where the electric part dominates, and within a rather narrow flux tube connecting the quarks. The energy flux extends farther out in the region surrounding the charges. Our data shows this in that the fiducial volume dependence of the volume sum rule is saturated more slowly than the transverse slice sum rule.

A second point is that it is reasonable to do this calculation with Wilson loops. Since one is always fighting the area law this has the advantage over Polyakov lines which must of course be as long as the time extent of the lattice. The dominant component, $E_{\parallel}$ turns out to be the most difficult component to extrapolate to large times.

420

Flux Distribution around q q̄

$$E^2 \approx -B^2$$

Non-Zero Energy; $E^2 + B^2 \neq 0$

Gluon Condensate differs
from vacuum value

$$E^2 \approx 0$$
$$B^2 \approx 0$$

Fig. 16. Schematic behavior of the flux distribution surrounding $q\bar{q}$

In this talk I presented a sample of our results. Lacking here is a discussion of scaling of our data. We are of course examining scaling and results will be presented later along with a more systematic analysis including the $\beta = 2.3$ data.

APPENDIX

Link integrals

Fluctuations were greatly suppressed by doing as many link integrals analytically as possible. Special problems occur depending on the proximity of one link to another. In this appendix we describe how to do all the link integrations in a plaquette and in a rectangular $n \times m$ Wilson loop ($n, m \geqslant 2$). There are further problems in correlation measurements when a plaquette is close or touching a Wilson loop. We do not treat such cases analytically but rather we drop the analytic integrals as necessary. These techniques are taken in large part from notes by B. Bunk. Programming was done independently.

A1. Character expansions

The basic technique used here is to expand integrands using group characters as basis functions. The character is given by the trace of the $(2j+1)$ dimensional rotation matrices.

$$\chi^{(j)}(U) = \sum_m D_{mm}^{(j)}(U) = \frac{\sin((2j+1)\psi)}{\sin\psi}; \quad j = 0, \tfrac{1}{2}, 1, \tfrac{3}{2}, \dots. \tag{1}$$

We parametrize group elements by an axis of rotation $\hat{n}$ and an angle of rotation about that axis denoted here by 2ψ.

$$U = \cos(\psi) + i\sin(\psi)\hat{n}\cdot\vec{\tau}, \tag{2}$$

and the group manifold is then the hypersurface of the 4-sphere and the invariant group integration measure is uniform on this manifold.

$$\int[dU] = \int_0^\pi \sin^2\psi d\psi \int d\hat{n},$$

$$\int d\hat{n} = \int_0^\pi \sin\theta d\theta \int_0^{2\pi} d\phi. \tag{3}$$

The orthogonality of characters follows.

$$\int_0^\pi \sin^2\psi d\psi \chi^{(j)}(U)\chi^{(j')}(U)$$

$$= \int_0^\pi d\psi \sin((2j+1)\psi)\sin((2j'+1)\psi) = \frac{\pi}{2}\delta_{j,j'}. \tag{4}$$

A useful recursion relation for characters is

$$\chi^{(j)}\chi^{(1/2)} = \chi^{(j+1/2)} + \chi^{(j-1/2)}. \tag{5}$$

We will make use of the following character expansion

$$e^{\frac{\beta}{2}\operatorname{tr}(U)} = \sum_j c_j(\beta)\chi^{(j)}(U); \quad c_j(\beta) = \frac{4j+2I_{2j+1}(\beta)}{\beta}, \tag{6}$$

where $I_{2j+1}(\beta)$ is the modified Bessel function. The sum is over all representations as indicated in Eq. (1).

A2. Single link integral

Consider the integral over the representation matrix $D_{mm'}^{(j)}(U)$

$$L_{mm'}^{(j)} \equiv \int[dU]D_{mm'}^{(j)}(U)e^{\frac{\beta}{2}\operatorname{tr}[UK^\dagger]}. \tag{7}$$

K is the sum of six 'staples' coupling to U in the action. The sum of SU(2) matrices in the $j = \frac{1}{2}$ representation is a multiple of an SU(2) matrix which we denote by V

$$K = bV; \quad b \equiv (\det K)^{1/2}, \tag{8}$$

which gives

$$L_{mm'}^{(j)} = \int [dU] D_{mm'}^{(j)}(U) e^{\frac{\beta b}{2} \text{tr}[UV^\dagger]}. \tag{9}$$

Group invariance allows us to write

$$L_{mm'}^{(j)} = \int [dU] D_{mm''}^{(j)}(U) e^{\frac{\beta b}{2} \text{tr}[U]} D_{m''m'}^{(j)}(V)$$

$$= \int [dU] \frac{1}{2j+1} \chi^j(U) e^{\frac{\beta b}{2} \text{tr}[U]} D_{mm'}^{(j)}(V) \tag{10}$$

We then make use of the character expansion, Eq. (6), and orthogonality, Eq. (4) to evaluate the integral

$$L_{mm'}^{(j)} = \frac{4\pi^2}{\beta b} I_{2j+1}(\beta b) D_{mm'}^{(j)}(V). \tag{11}$$

Applying this result for $j = 0$ and $\frac{1}{2}$ gives the desired form of the one link integral

$$\int [dU] U e^{\frac{\beta}{2} \text{tr}[UK^\dagger]} = \frac{I_2(\beta b)}{I_1(\beta b)} V \int [dU] e^{\frac{\beta}{2} \text{tr}[UK^\dagger]}. \tag{12}$$

The effect of this identity when applied to a simulation is to replace a link U occurring in the Wilson loop by a corresponding sum of 'staples' K. Since K involves 18 links, one can expect the fluctuations of the ensemble of K's to be suppressed compared to a single link U in each measurement.

The result is useful when a subsequent analytic integration does not involve one of the links in K. For example this will work for those links that make up the sides of a Wilson loop as long as one link on each corner is left in its original form. This result must be generalized to handle the four links in a plaquette and the the two links that form corners.

A3. Plaquette integral

Consider the following four-link integral

$$Z(\gamma, \beta) \equiv \int [dU_1 dU_2 dU_3 dU_4] e^{-S}, \tag{13}$$

where

$$-S \equiv \left(\frac{\gamma}{2} \text{tr} [U_4^\dagger U_3^\dagger U_2 U_1] = \frac{\beta}{2} \sum_{k=1}^{4} \text{tr} [U_k K_k^\dagger] \right). \tag{14}$$

We have displayed explicitly the dependence of the action on the links making up a particular plaquette. Each K_k matrix is the sum of six staples. We apply the character expansion to each of the five terms in the exponential

$$Z(\gamma, \beta) = \int \left[\prod_l dU_l\right] \sum_j c_j(\gamma)\chi^{(J)}(U_4^\dagger U_3^\dagger U_2 U_1) \prod_{k=1}^4 \sum_{j_k} c_{j_k}(\beta k_k)\chi^{(j_k)}(U_k V_k^\dagger). \tag{15}$$

All integrals can be done making use of the orthogonality of the group integration.

$$\int [dU]D_{mn}^{(j)}(U)^* D_{m'n'}^{(j')}(U) = \frac{2\pi^2}{2j+1}\delta_{jj'}\delta_{mm'}\delta_{nn'} \tag{16}$$

Using this result we find for example

$$\int [dU_1]\chi^{(J)}(U_4^\dagger U_3^\dagger U_2 U_1)\chi^{(j_1)}(U_1 V_1^\dagger) = \frac{2\pi^2}{2j+1}\delta_{jj_1}\chi^{(J)}(U_4^\dagger U_3^\dagger U_2 V_1). \tag{17}$$

Applying this result for all four links reduces Eq. (13) to a single sum:

$$Z(\gamma, \beta) = \sum_j c_j(\gamma)\frac{(2\pi^2)^4}{(2j+1)^4}\prod_{k=1}^4 c_j(\beta b_j)\chi^{(J)}(V_4^\dagger V_3^\dagger V_2 V_1). \tag{18}$$

Pulling this together, we get the result

$$\int\left[\prod_l dU_l\right]\tfrac{1}{2}\operatorname{tr}(U_4^\dagger U_3^\dagger U_2 U_1)e^{-S} = \frac{\left.\dfrac{\partial Z(\gamma, \beta)}{\partial \gamma}\right|_{\gamma=\beta}}{Z(\beta, \beta)}\int\left[\prod_l dU_l\right]e^{-S}. \tag{19}$$

We need the expansion coeffcients $c_j(\beta)$, Eq. (6) and the first derivative with respect to β, $c_j'(\beta)$. These are proportional to modified Bessel functions and can be evaluated by recursion only in the direction of decreasing index. We employed the following relations which follow from standard Bessel function recursion relations:

$$\tilde{c}_j = \tilde{c}_{j+1/2}' + \frac{2j+3}{\beta}\tilde{c}_{j+1/2},$$

$$\tilde{c}_j' = \frac{2j}{\beta}\tilde{c}_{j+1/2}' + \left(1 + \frac{2j(2j+3)}{\beta^2}\right)\tilde{c}_{j+1/2}, \tag{20}$$

where

$$\tilde{c}_j \equiv \frac{c_j}{2j+1}; \quad \tilde{c}_j' \equiv \frac{c_j'}{2j+1}. \tag{21}$$

A4. Corner integral

Consider the integral over two links that form a corner

$$\langle U_2 U_1 \rangle \equiv \frac{1}{Z} \int [dU_1 dU_2] U_2 U_1 e^{-S},$$

$$Z \equiv \int [dU_1 dU_2] e^{-S}, \tag{22}$$

where the relevent terms in the action are

$$-S \equiv \frac{\beta}{2} (\text{tr}\,(W^\dagger U_2 U_1) + b_1 \,\text{tr}\,(U_1 V_1^\dagger) + b_2 \,\text{tr}\,(U_2 V_2^\dagger)). \tag{23}$$

Z can be evaluated immediately using the above methods

$$Z = \sum_j \frac{(2\pi^2)^2}{(2j+1)^2} \, c_j(\beta) c_j(\beta b_1) c_j(\beta b_2) \chi^{(j)}(P), \tag{24}$$

where

$$P \equiv W^\dagger V_2 V_1. \tag{25}$$

Applying the character expansion to the three terms in the action we obtain

$$\langle U_2 U_1 \rangle = \frac{1}{Z} \sum_{j_1 j_2 j} c_j(\beta) c_{j_1}(\beta b_1) c_{j_2}(\beta b_2)$$

$$\times \int [dU_1 dU_2] U_2 U_1 \chi^{(j)}(W^\dagger U_2 U_1) \chi^{(j_1)}(U_1 V_1^\dagger) \chi^{(j_2)}(U_2 V_2^\dagger). \tag{26}$$

We can immediately do one integral and one sum:

$$\langle U_2 U_1 \rangle = \frac{1}{Z} \sum_{jj'} \frac{2\pi^2}{2j'+1} c_j(\beta) c_{j'}(\beta b_1) c_{j'}(\beta b_2)$$

$$\times W \int [dU] U \chi^{(j)}(U) \chi^{(j')}(U P^\dagger). \tag{27}$$

The remaining integral and one more sum can be done by expressing the U matrix in the integrand as a function of P and invariants. This can by done by a judicious choice of coodinates. Define a parametrization of U and P

$$U = I \cos \psi_u + i\hat{u} \cdot \vec{\tau} \sin \psi_u,$$

$$P = I \cos \psi_p + i\hat{p} \cdot \vec{\tau} \sin \psi_p. \tag{28}$$

We need

$$\text{Tr}\,[U] = 2 \cos \psi_u,$$

$$\text{Tr}\,[U P^\dagger] = 2(\cos \psi_u \cos \psi_p + \sin \psi_u \sin \psi_p \hat{u} \cdot \hat{p}). \tag{29}$$

Let us further parametrize $\hat{u}$:

$$\hat{u} = \hat{e}_3 \cos \theta_u + \hat{e}_2 \sin \theta_u \sin \phi_u + \hat{e}_1 \sin \theta_u \cos \phi_u. \qquad (30)$$

Now choose $\hat{e}_3 = \hat{p}$. It is clear that the ϕ_u integration will kill the $\hat{e}_1$ and $\hat{e}_2$ contributions and they are henceforth dropped. Therefore the surviving terms in U can be written

$$U = I \cos \psi_u + i\hat{p} \cdot \vec{\tau} \cos \theta_u \sin \psi_u. \qquad (31)$$

Using Eqs. (29), (30) we obtain the desired form for U:

$$U = \chi^{(1/2)}(U)A + \chi^{(1/2)}(P^\dagger U)B, \qquad (32)$$

where

$$A \equiv \frac{I - \frac{1}{2} P \chi^{(1/2)}(P)}{2 - \frac{1}{2} \chi^{(1/2)}(P)^2},$$

$$B \equiv \frac{P - \frac{1}{2} I \chi^{(1/2)}(P)}{2 - \frac{1}{2} \chi^{(1/2)}(P)^2}. \qquad (33)$$

We apply this result to the integral occurring in Eq. (27)

$$\int [dU] U \chi^{(j)}(U) \chi^{(j')}(UP^\dagger) = A \int [dU] \chi^{(1/2)}(U) \chi^{(j)}(U) \chi^{(j')}(UP^\dagger)$$

$$+ B \int [dU] \chi^{(1/2)}(UP^\dagger) \chi^{(j')}(UP^\dagger) \chi^{(j)}(U). \qquad (34)$$

We can use the recursion relation for characters, Eq. (5), to obtain an integrand involving only two characters as factors. Once it is down to a two character integration, Eq. (17) can be used to evaluate the integral. We quote the final result

$$\langle U_2 U_1 \rangle = \frac{1}{Z} \sum_j \frac{(2\pi^2)^2}{(2j+1)^2} c_j(\beta b_1) c_j(\beta b_2) \left\{ W c_j' \chi^{(j)}(P) \right.$$

$$\left. + c_j \frac{[V_2 V_1 - W \frac{1}{2} \chi^{(1/2)}(P)] [(j+1)\chi^{(j-1/2)}(P) - j\chi^{(j+1/2)}(P)]}{\beta(1 - \frac{1}{4} \chi^{(1/2)}(P)^2)} \right\}. \qquad (35)$$

REFERENCES

[1] M. Fukugita, I. Niuya, *Phys. Lett.* **132B**, 374 (1983).

[2] J. Flower, S. Otto, *Phys. Lett.* **160B**, 128 (1985).

[3] R. Sommer, *Nucl. Phys.* **B291**, 673 (1987).

[4] J. Wosiek, R. W. Haymaker, *Phys. Rev. Rapid Comm.* **D36**, 3297 (1987); see also J. Wosiek, *Nucl. Phys.* B (Proc. Suppl.) **4**, 52 (1988).

[5] I. H. Jorysz, C. Michael, *Nucl. Phys.* **B302**, 448 (1987).

[6] R. Sommer *Nucl. Phys.* **B306**, 180 (1988).

[7] S. Perantonis, A. Huntley, C. Michael, Liverpool preprint LTH227, December 1988; see also S. Perantonis, *Nucl. Phys.* B (Proc. Suppl.) **9**, 249 (1989).

[8] C. Michael, *Nucl. Phys.* **B280** **[FS18]**, 13 (1987).

[9] M. Creutz, *Phys. Rev.* **D36**, 515 (1987).

[10] G. Parisi, R. Petronzio, F. Rapuano, *Phys. Lett.* **128B**, 418 (1983).

[11] F. Gutbrod, *Z. Phys.* **C30**, 585 (1986).

[12] B. Bunk, unpublished notes.

[13] J. D. Bjorken, *Phys. Rev.* **D27**, 140 (1983); *Phys. Rev.* **D27**, 399 (1984).

[14] A. Chodos, R. Jaffe, K. Johnson, C. Thorn, V. Weisskopf, *Phys. Rev.* **9**, 3471 (1974).

[15] K. Johnson, *Acta Phys. Pol.* **B6**, 865 (1975).

[16] M. Lüscher, G. Münster, P. Weisz, *Nucl. Phys.* **B180** **[FS2]**, 1 (1981).

[17] C. Peterson, L. Sköld, *Nucl. Phys.* **B255**, 365 (1985).